

Highly Efficient Ternary Solar Cells of 10.2% with Core/Shell Quantum Dots via FRET Effect

Yong Woon Han, Sung Jae Jeon, Jun Young Choi, Joo Hyun Kim, and Doo Kyung Moon*

Ternary organic solar cells (OSCs) with the efficiency over 10% are fabricated as an inverted structure with core/shell type quantum dots (QDs) as third component. Förster resonance energy transfer occurs due to overlap between the emission range ($\lambda_{em} = 500\text{--}800\text{ nm}$) of InP/ZnS QDs and the absorption range ($\lambda_{abs} = 550\text{--}800\text{ nm}$) of PTB7-Th donor polymer. InP/ZnS QDs increase the photocurrent of the hybrid active layer via the strong emission properties of ZnS shells surrounding the InP core QDs, which transfer photon energy to PTB7-Th (UV-vis spectroscopy and photoluminescence). X-ray photoelectron spectroscopy (XPS) depth profiling reveals that InP/ZnS QDs are distributed on the surface of the hybrid active layer, while grazing-incidence wide-angle X-ray scattering (GIWAXS) analysis reveals that these QDs enhance the crystalline structure of the hybrid active layer. The incorporation of an ethanedithiol (EDT)-modified ZnO layer as an electron transport layer enhances the carrier transport and decreases carrier recombination, providing a uniform morphology and surface potential favorable for electron extraction and transport, as indicated by atomic force microscopy and electrostatic force microscopy analyses. Due to the synergistic effects of InP/ZnS QDs and the EDT-modified ZnO layer, the power conversion efficiency (PCE) is 10.2% via the enhancement in short-circuit current density (J_{sc}) from 17.4 to 18.4 mA cm^{-2} and fill factor (FF) from 67.2 to 69.3%.

bulk-heterojunction (BHJ) OSCs based on novel polymer donors and fullerene-based acceptors, which achieve efficiencies of more than 11% through the modification of materials and device structures.^[4–10]

Binary OSCs based on one donor and one acceptor generate excitons within the optical ranges of the donor and acceptor, and then exhibit photovoltaic properties of charge dissociation and charge transport.^[11] Currently, binary active layers based on one donor and one acceptor have limited absorption properties and have limitations such as low charge transporting property.^[12–14]

As an approach to overcome these limitations, ternary solar cells – which introduce a third component to the binary active layer – are attracting attention.^[15–21] In general, the mechanisms by which the third component (introduced to the binary active layer) improves performance are as follows: energy transfer,^[22–24] charge transfer,^[25–27] parallel structure, or alloy structure.^[28,29] The ternary structure formed by introducing a third component can improve the photo-

voltaic performance by enhancing photon harvesting or tuning built-in potential or optimizing morphology.

Ternary solar cells have the following advantages: 1) it is possible to easily manufacture a device by introducing a single active layer in a binary solar cell; 2) the introduction of a third component with different absorption properties than the existing donor/acceptors can overcome the limited optical properties of organic semiconductor-based active layers^[22,30]; and 3) introducing a third component can facilitate carrier transport by forming favorable energy levels with the existing donor/acceptor.^[16,26]


One of the most notable methods is the mechanism that improves the performance by increasing the photocurrent through energy transfer. This mechanism can overcome the optical limitations of the existing medium and the long wavelength absorption properties of the active layer by introducing a third component with primarily short wavelength absorption properties. Zhang et al. introduced squaraine (SQ) as an energy acceptor in a poly[N-9'-heptadecanyl-2,7-carbazole-alt-5,5-(4',7'-di-2-thienyl-2',1',3'-benzothiadiazole)] (PCDTBT) and phenyl-C₇₁-butyric-acid-methyl ester (PC₇₁BM) based binary active layer and reported an improvement in power conversion

1. Introduction

Organic solar cells (OSCs) based on organic semiconductors are currently an attractive field of research due to their advantages such as solution processing, ease of fabrication, and potential for use in flexible devices.^[1–3] Many studies have been conducted on

Y. W. Han, S. J. Jeon, J. Y. Choi, Prof. D. K. Moon
Nano and Information Materials Lab. (NIMs Lab.)
Department of Materials Chemistry and Engineering
Konkuk University
120 Neungdong-ro, Gwangjin-gu, Seoul 05029, South Korea
E-mail: dkmoon@konkuk.ac.kr

Prof. J. H. Kim
Organic Opto-Electronic Materials Lab. (OOM Lab.)
Department of Polymer Engineering
Pukyong National University
365 Sinseon-ro, Nam-gu, Busan 48547, South Korea

 The ORCID identification number(s) for the author(s) of this article can be found under <https://doi.org/10.1002/solr.201800077>.

DOI: 10.1002/solr.201800077

efficiency (PCE) from 6.54 to 7.62%. This facilitated energy transfer from the donor PCDTBT to the third component (SQ), resulting in an improvement in PCE due to the increase in photocurrent.^[23]

Recently, a method for enhancing the performances of OSCs by incorporating the advantages of inorganic semiconductors – such as their unique optical properties and high mobility properties – into OSCs has been attracting attention.^[31,32] In particular, inorganic semiconductor quantum dots (QDs) have outstanding optical properties and possess suitable properties for the fabrication of photovoltaic devices via facile solution processing including large extinction coefficients, high emission properties, and quantum-size-effect band gap tunability.^[33–37] Ma et al. fabricated hybrid solar cells with PDTPBT as the donor and QDs of $\text{PbS}_x\text{Se}_{1-x}$ as the acceptor to form an ideal phase that exhibited PCE of up to 5.5%.^[38] Guo et al. introduced $\text{CuInS}_2/\text{ZnS}$ QDs, which formed a unique energy level with the third component in a binary active layer with the PCDTBT donor and PC_{71}BM acceptor, exhibiting improved charge generation and charge transport characteristics. In addition, they reported a PCE of 7.19%, which was an improvement of 21.6% compared to the existing PCE.^[39]

Most studies have attempted to improve performance through the charge transfer mechanism by introducing QDs as electron acceptors or as third components to make use of their outstanding optical properties. In particular, introducing QDs with strong emission properties as the third component to facilitate energy transfer rather than for charge transfer can improve the optical properties of organic-based binary active layers.^[40]

In this study, quantum dots with indium phosphide (InP) core and zinc sulfide (ZnS) shell (InP/ZnS QDs) were introduced as a

third component for energy transfer to a binary active layer containing poly[4,8-bis(5-(2-ethylhexyl)thiophen-2-yl)benzo[1,2-b;4,5-b']dithiophene-2,6-diyl-alt-(4-(2-ethylhexyl)-3-fluorothieno[3,4-b]thiophene)-2-carboxylate-2,6-diyl] (PTB7-Th) as the donor and PC_{71}BM as the acceptor. Hybrid ternary solar cells with an inverted structure were fabricated based on this organic–inorganic hybrid active layer.

InP/ZnS QDs have stronger emission properties than the core InP QDs used in our previous study^[40] due to the introduction of ZnS shells. The emission range of the InP/ZnS QDs overlapped with the absorption range of the PTB7-Th donor, which improved the photocurrent of the active layer through the Förster resonance energy transfer (FRET) mechanism. This phenomenon was confirmed by absorption and emission analyses. By X-ray photoelectron spectroscopy (XPS) depth profiling and grazing-incidence wide-angle X-ray scattering (GIWAXS) analysis, the InP/ZnS QDs were found to be distributed on the surface of the hybrid active layer, which enhanced crystallinity of active layer. The introduction of a modified ZnO layer by 1, 2-ethanedithiol (EDT) treatment formed a favorable structure for carrier transport. This was confirmed by analyzing the surface morphology (by atomic force microscopy (AFM)) and surface potential (by electrostatic force microscopy (EFM)). Hence, both, short-circuit current density (J_{SC}) and, short-circuit current density (FF) improved through the synergistic effect of incorporating InP/ZnS QDs and EDT-modified ZnO layers in hybrid solar cells, resulting in a high PCE of 10.2%.

2. Results and Discussion

Figure 1 shows the structure of the device fabricated in this study (Figure 1a) and the structures of the materials used (Figure 1b–

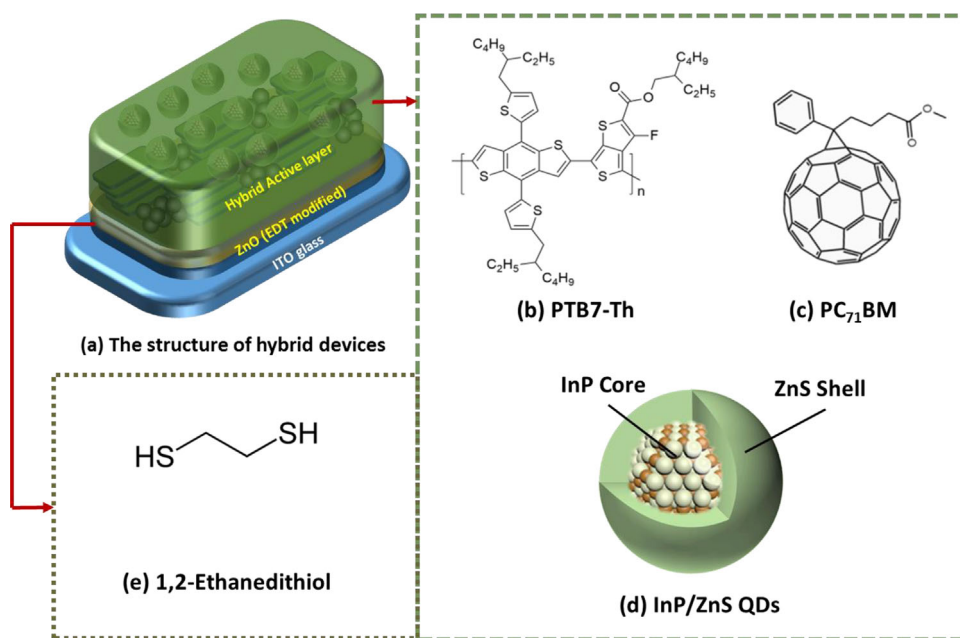


Figure 1. Schematic images of materials in hybrid solar cells and structure with condition of fabricated hybrid solar cells.

e). As shown in Figure 1a, the device was fabricated with an inverted structure (ITO/ZnO/active layer/MoO₃/Ag). The active layer contained PTB7-Th (Figure 1b) as the donor and PC₇₁BM (Figure 1c) as the acceptor. The structure of the InP/ZnS QDs introduced in the photoactive layer for energy transfer is shown in Figure 1d. Figure 1e shows the structure of EDT used to modify the surface of the ZnO layer, which was introduced as the ETL.

Figure 2a shows TEM images of InP QDs and InP/ZnS QDs. The sizes of the InP QDs and InP/ZnS QDs were 2.89 and 3.52 nm, respectively; they formed larger QDs by surface passivation of ZnS shells. Figure 2b shows the optical properties of InP/ZnS QDs (introduced in this study) and InP QDs (used in our previous studies). The absorption of InP/ZnS QDs ($\lambda_{\text{abs}} \approx 650$ nm) was blue-shifted relative to that of InP QDs ($\lambda_{\text{abs}} \approx 700$ nm). The emission of InP/ZnS QDs ($\lambda_{\text{em}} = 500\text{--}800$) was also blue-shifted ($\approx \lambda_{\text{shift}} = 50$ nm) relative to that of InP QDs ($\lambda_{\text{em}} = 550\text{--}800$ nm). InP/ZnS QDs exhibited higher emission than InP QDs. This is because the ZnS shells reduce charge trapping by removing the surface defects of InP QDs to form uniform surfaces.^[41,42] The blue shift in the optical properties is due to the ZnS shells covering the core.^[43,44] Furthermore, the absorption band of InP/ZnS QDs was weaker and the emission band was stronger than those of InP QDs. This is because the trap sites on the core-type InP QDs surface can be passivated by the introduction of ZnS shells, which reduces carrier recombination and thus greatly increases emission.^[45]

Figure 2c shows surface images (Figure 2c-1 and c-2) of the BHJ active layer incorporated on the ETL (ZnO layer or EDT-modified ZnO layer). In recent years, several studies have

reported improvements in photovoltaic performance by removing surface defects and creating uniform morphologies through ZnO surface treatment with several polar solvents.^[46–50] In this study, the EDT-modified ZnO layer presented a smoother surface than the ZnO layer. This is consistent with the tendency in the study of Gao et al. to reduce carrier recombination by removing vacancies (oxygen, hydroxy groups, etc.) present on the ZnO surface by EDT treatment.^[48]

Figure 2c-3 and c-4 show surface images of the BHJ + QDs active layer (containing InP/ZnS QDs) and the BHJ active layer, respectively, incorporated on the ETL (ZnO layer or EDT-modified ZnO layer). A rough surface was formed by the introduction of InP/ZnS QDs (Figure 2c-3). The active layer (Figure 2c-4) introduced on the EDT-modified ZnO layer showed a uniform surface due to EDT treatment. This means that the rough morphology formed by the introduction of InP/ZnS QDs can be controlled by the EDT-modified ZnO layer, imparting a uniform morphology.

Table 1 shows the device structures fabricated in this study. Device 1 was a bulk-heterojunction device (PTB7-Th + PC₇₁BM, referred to as “BHJ”) with PTB7-Th and PC₇₁BM as the active layers incorporated on the ZnO ETL. In Device 2, EDT-modified ZnO replaced the ZnO layer that was used in Device 1. Devices 3 and 4 were hybrid devices (PTB7-Th + PC₇₁BM + InP/ZnS QDs, referred to as “BHJ + QDs”) incorporating InP/ZnS QDs in the photoactive layers of Devices 1 and 2, respectively.

Figure 3 shows the current density–voltage (J – V) (Figure 3a) and EQE properties of the fabricated hybrid solar cell devices (Figure 3b). As shown in Figure 3a, Device 1 (fabricated with a BHJ active layer) had a PCE performance of 9.1% ($J_{\text{SC}} = 17.4$

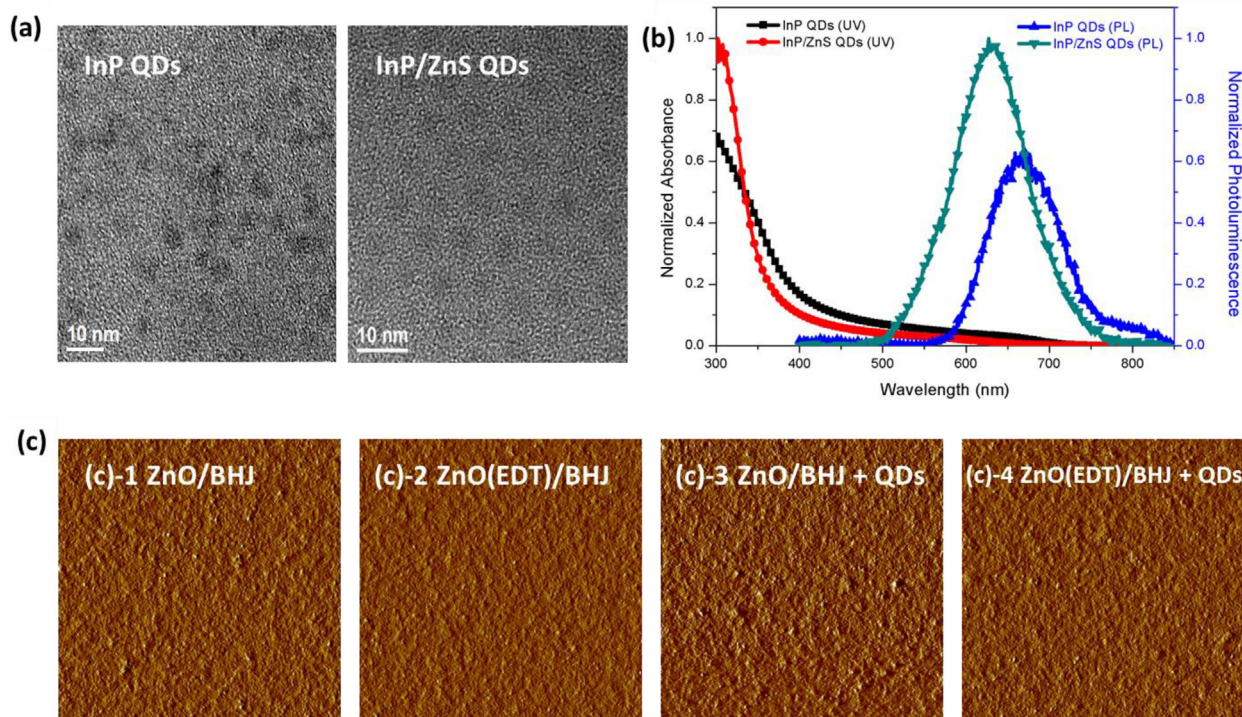


Figure 2. a) TEM images of InP QDs (left) and InP@ZnS QDs (right). b) Absorption and emission characteristics of InP QDs and InP@ZnS QDs. c) Phase images of fabricated hybrid active layer: (c)-1: ZnO/BHJ, (c)-2: ZnO(EDT)/BHJ, (c)-3: ZnO/BHJ + QDs, and (c)-4: ZnO(EDT)/BHJ + QDs.

Table 1. Photovoltaic performances of BHJ (PTB7-Th + PC₇₁BM) + QDs (InP/ZnS QDs) hybrid solar cells.

Device structure	J_{SC} [mA cm^{-2}]	V_{OC} [V]	FF [%]	PCE [%]
Device 1 (ZnO/BHJ)	17.4	0.777	67.2	9.1 ^{a)}
Device 2 (ZnO (EDT)/BHJ)	18.0	0.798	67.5	9.7 ^{a)}
Device 3 (ZnO/BHJ + QDs)	18.3	0.798	66.2	9.7 ^{a)}
Device 4 (ZnO (EDT)/BHJ + QDs)	18.4	0.798	69.3	10.2 ^{a)}

^{a)}The average values and deviations were obtained from 10 devices.

mA cm^{-2} , $V_{OC} = 0.777$ V, and FF = 67.2%). Device 2 (with EDT-modified ZnO replacing the ZnO layer in Device 1) showed PCE of 9.7% ($J_{SC} = 18.0$ mA cm^{-2} , $V_{OC} = 0.798$ V, and FF = 67.5%). Device 3 (fabricated with InP/ZnS QDs in the layers of Device 1) exhibited PCE of 9.7% ($J_{SC} = 18.3$ mA cm^{-2} , $V_{OC} = 0.798$ V, and FF = 66.2%). Finally, Device 4 (with both InP/ZnS QDs and EDT-modified ZnO layer) had the highest performance with PCE = 10.2% ($J_{SC} = 18.4$ mA cm^{-2} , $V_{OC} = 0.798$ V, and FF = 69.3%). The performances of optimized concentration with InP/ZnS QDs (Figure S1a, Supporting Information) and the hybrid solar cells fabricated from BHJ + InP QDs and EDT-modified ZnO layer (Figure S1b, Supporting Information) are shown in Figure S1, Table S1, and S2, Supporting information. Introduction of the InP QDs and EDT-modified ZnO layer improved J_{SC} over that of Device 1 but showed lower performance than that of the device containing InP/ZnS QDs. This is the reason that both InP QDs and InP/ZnS QDs could offer additional photon energy via FRET effect. Because of the emission intensity of InP QDs was lower than InP/ZnS QDs, the higher energy transferred to PTB7-Th from InP/ZnS QDs rather than InP QDs.

As shown in Table 1, when InP/ZnS QDs were introduced in the active layer, J_{SC} increased from 17.4 (Device 1) to 18.3 mA cm^{-2} (Device 3). Meanwhile, FF decreased slightly from 67.2 (Device 1) to 66.2% (Device 3). Due to EDT treatment of the ZnO layer, J_{SC} increased from 17.4 (Device 1) to 18.0 mA cm^{-2} (Device 2), while FF increased from 67.2 (Device 1) to 67.5% (Device 2). As a result, InP/ZnS QDs improved J_{SC}

and EDT treatment improved J_{SC} and FF. When both InP/ZnS QDs and the EDT-modified ZnO layer were introduced, J_{SC} increased from 17.4 (Device 1) to 18.4 mA cm^{-2} (Device 4), while FF increased from 67.2 (Device 1) to 69.3% (Device 4). As a result, PCE improved from 9.1 to 10.2%. This is due to the synergistic effects of introducing both InP/ZnS QDs and the EDT-modified ZnO layer on the improvement of J_{SC} and FF. The V_{OC} of Devices 2–4 were slightly enhanced from 0.777 to 0.798 V because of introducing InP/ZnS QDs and EDT treatment by the strengthening of internal built-in potential.

As shown in Figure 3b, the calculated J_{SC} values obtained by measuring the EQE were 15.27, 15.92, 16.47, and 16.78 mA cm^{-2} for Devices 1–4, respectively. Especially, the devices with InP/ZnS QDs showed higher intensity in the region of 300–400 nm because of higher absorption properties of InP/ZnS QDs in this region. This is consistent with the current density–voltage property shown in Figure 3a.

In Figure 4a, the optical properties of the materials used in the hybrid active layer are shown. The properties agree with the emission ranges of both the InP QDs and InP/ZnS QDs rather than the main absorption range ($\lambda_{abs} = 550\text{--}800$ nm) of the PTB7-Th donor polymer used in the hybrid active layer. In this region, energy transfer can occur from the InP/ZnS QDs to PTB7-Th via FRET at the wavelength where the emission of the InP/ZnS QDs overlaps with the absorption of PTB7-Th. The FRET effect is a photoconversion mechanism in which energy transfer occurs due to overlap of the specific optical ranges of photoactive materials. Sensitizers can be used as the third component in photoactive materials in OSCs to extend the spectral absorption range.^[51,52] In particular, Zhao et al. reported that hybrid OSCs containing sensitizers with near-infrared absorption properties were fabricated on PCDTBT- and PC₇₁BM-based active layers and that the absorption properties were extended by energy transfer. In addition, they reported that the PCE improved from 4.91 to 6.39%.^[53]

Photoluminescence (PL) characteristics of pure InP/ZnS QDs, mixture of PTB7-Th:InP/ZnS QDs, and pure PTB7-Th was performed with respect to various mixing ratio to confirm FRET effect from InP/ZnS QDs to PTB7-Th (shown in Figure 4b).^[54] InP/ZnS QDs (FRET donor) showed high emission intensity

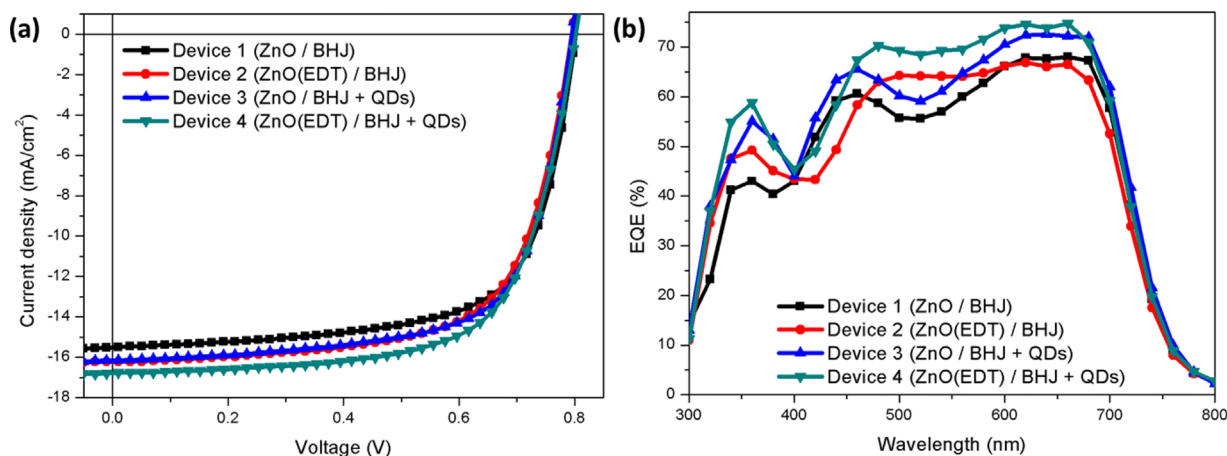


Figure 3. a) Current density–voltage (J – V) characteristics and b) external quantum efficiency characteristics of fabricated hybrid solar cells.

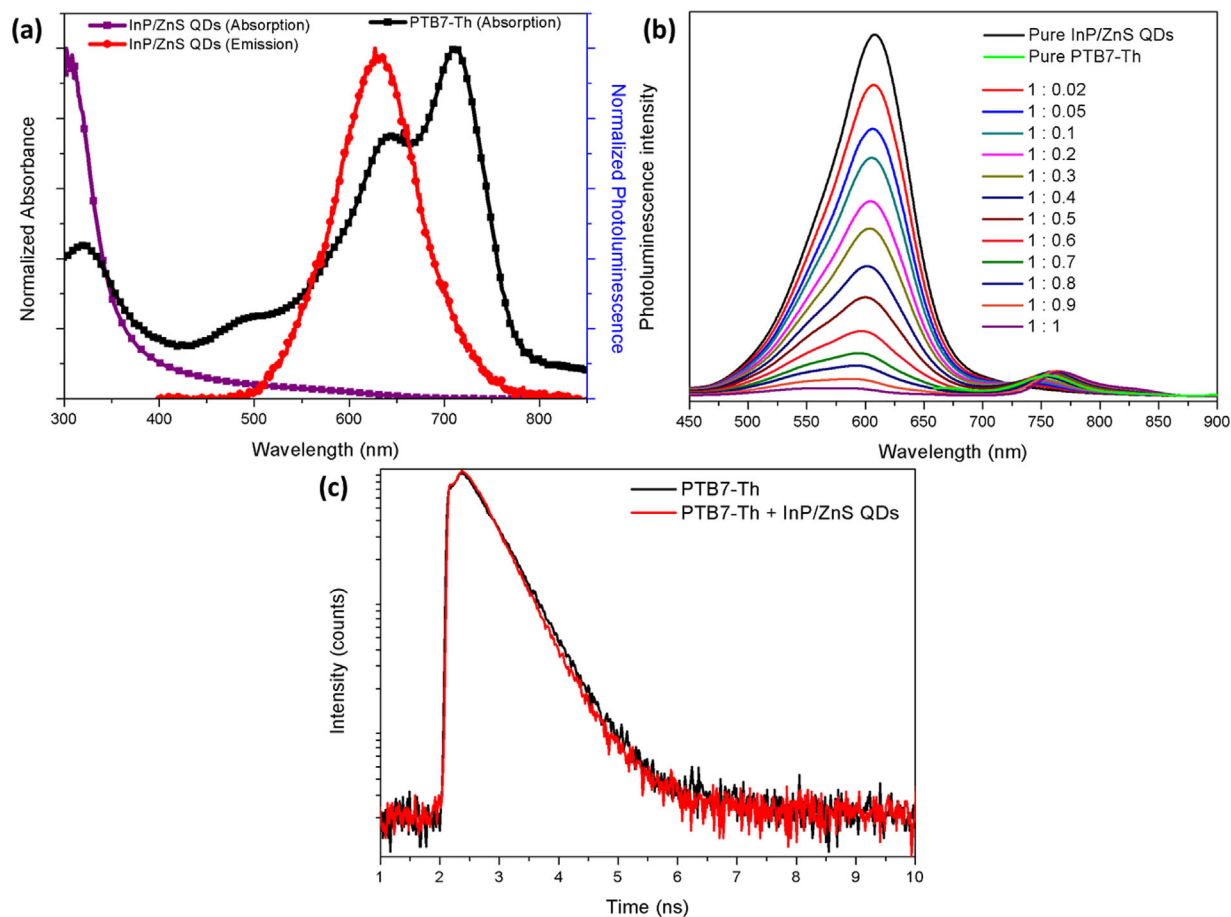


Figure 4. a) Optical characteristics of PTB7-Th and InP/ZnS QDs. b) Photoluminescence characteristics of InP/ZnS QDs and PTB7-Th mixture in various ratio. c) Time-resolved photoluminescence characteristics of PTB7-Th without and with InP/ZnS QDs.

($\lambda_{\max} = 610$ nm). When PTB7-Th (FRET acceptor) introduced slightly, the emission intensity of InP/ZnS QDs dropped down and the emission intensity of PTB7-Th peak (≈ 775 nm) increased. When the ratio of InP/ZnS QDs:PTB7-Th is over 1:0.5, the emission intensity of PTB7-Th peak showed higher intensity rather than that of the pure PTB7-Th. This is because energy transfer via FRET effect appeared from FRET donor to FRET acceptor.

To prove energy transfer between InP/ZnS QDs and PTB7-Th via FRET effects, the Förster radius (R_0) was calculated (shown in Figure S2a–e, Supporting Information). FRET donor can transfer energy to FRET acceptor in the overlap region located within Förster radius that the typical length scale of <10 nm where FRET energy transfer can occur. The Förster radius was calculated with Equations S(1)–S(3), Supporting Information and some factors.^[54,55] The calculated Förster radius (R_0) = 2.063 nm (details are shown in Supporting Information). This result prove that the energy transfer from InP/ZnS QDs to PTB7-Th is favorable via FRET effect.

To further verify the energy transfer from InP/ZnS QDs to PTB7-Th, the time-resolved PL properties of films are shown in Figure 4c, monitored at $\lambda_{\text{em}} = 600\text{--}650$ nm under 470 nm excitation. The average lifetime of carriers was characterized

by previous literature.^[56] The measured lifetime of PTB7-Th was 0.517 ns and PTB7-Th + InP/ZnS QDs was 0.464 ns, respectively. As shown in Figure S2a–e, Supporting Information, PTB7-Th and InP/ZnS QDs were mixed within Förster radius. The emission decay profile of PTB7-Th is more obvious by mixing with InP/ZnS QDs. This phenomena obviously suggest that the harvested energy transferred from InP/ZnS QDs to PTB7-Th due to overlap of optical properties within Förster radius.^[23,57]

Figure 5 show the optical properties of hybrid photoactive layer. In our previous study, InP QDs were introduced to an active layer consisting of PTB7 and PC₇₁BM to improve the photovoltaic properties. The emission range of the InP QDs overlapped the absorption range of PTB7 (a polymer donor) and the absorption property of the InP QDs was added to the absorption properties of the original PTB7 donor. As a result, the performance improved due to the expanded absorption properties. The InP/ZnS QDs used in this study had better emission properties than the InP QDs (Figure 4a) allowing better energy transfer to PTB7-Th.

Figure 5a and b show the absorption properties when InP QDs and InP/ZnS QDs were introduced in pristine PTB7-Th and the BHJ (PTB7-Th + PC₇₁BM) active layer, respectively. PTB7-Th

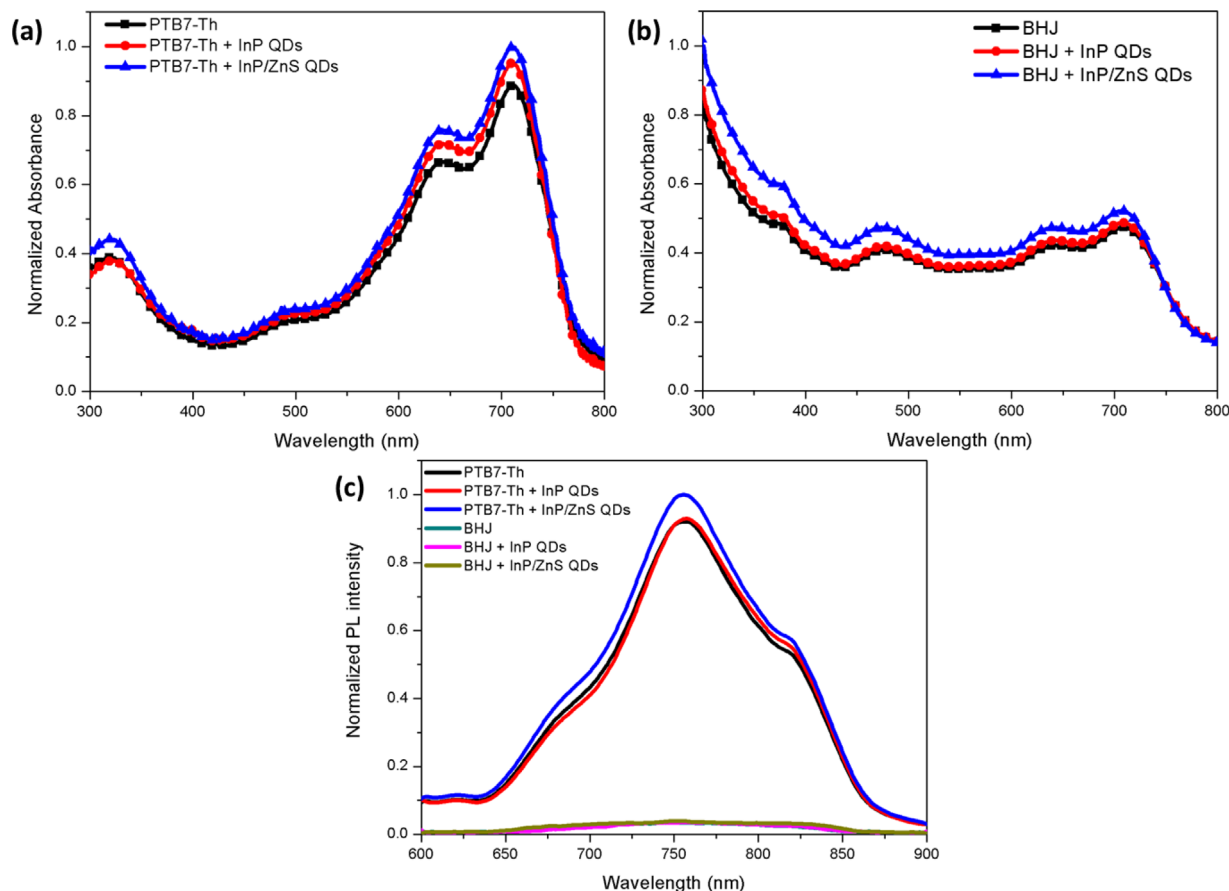


Figure 5. a) Absorption characteristics of PTB7-Th only and with InP QDs or InP/ZnS QDs. b) Absorption characteristics of BHJ only and with InP QDs or InP/ZnS QDs. c) Photoluminescence characteristics of PTB7-Th & BHJ only and with InP QDs or InP/ZnS QDs.

has a main absorption at $\lambda_{\text{abs}} = 550\text{--}800\text{ nm}$, as shown in Figure 4a. When InP QDs and InP/ZnS QDs were introduced in PTB7-Th, the absorption intensity improved without an absorption shift. The absorption intensity of the hybrid active layer containing InP/ZnS QDs increased more than that containing InP QDs. When InP QDs and InP/ZnS QDs were introduced in the BHJ active layer, the absorption with InP/ZnS QDs was more intense than that with InP QDs. This is due to energy transfer from InP/ZnS QDs to PTB7-Th resulting from the overlap of the emission range ($\lambda_{\text{em}} = 500\text{--}800\text{ nm}$) of the InP/ZnS QDs and the absorption range ($\lambda_{\text{abs}} = 550\text{--}800\text{ nm}$) of PTB7-Th. As a result, the stronger emission of the InP/ZnS QDs with ZnS shells relative to that of the InP QDs significantly increased the absorption properties of PTB7-Th through the FRET effect.

Figure 5c shows the PL characteristics when InP QDs and InP/ZnS QDs were introduced in a pristine PTB7-Th layer and the BHJ active layer, respectively. Pristine PTB7-Th and PTB7-Th containing QDs (InP QDs and InP/ZnS QDs) showed maximum emission intensities at $\approx \lambda_{\text{em}} = 760\text{ nm}$. The emission intensity of the PTB7-Th containing InP QDs was higher than that of pristine PTB7-Th. The highest emission intensity was obtained when InP/ZnS QDs were introduced in PTB7-Th. This difference is because the additional energy absorbed by the main donor (PTB7-Th polymer) was transferred from the InP

QDs and InP/ZnS QDs via FRET effects, creating additional carriers.

The BHJ active layer showed lower emission intensity than pristine PTB7-Th. This decrease was due to PL quenching by PC₇₁BM. When InP QDs or InP/ZnS QDs were introduced in the BHJ active layer, all samples showed a maximum emission intensity at $\lambda_{\text{em}} = \approx 730\text{ nm}$. The BHJ active layer containing InP QDs showed lower emission intensity than the BHJ active layer; the BHJ active layer containing InP/ZnS QDs showed the lowest emission intensity. PL quenching rates were 95.66% (BHJ), 96.16% (BHJ + InP QDs), and 96.51% (BHJ + InP/ZnS QDs); the highest PL quenching rate was obtained when InP/ZnS QDs were introduced.

InP QDs and InP/ZnS QDs were introduced to the BHJ active layer to enhance the absorption properties of PTB7-Th through energy transfer by creating additional carriers. In addition, the introduction of QDs contributed to enhanced carrier transport by improving the PL quenching property. As shown in Figure 3 and Table 1, the introduction of InP QDs and InP/ZnS QDs is consistent with the improvement of J_{SC} . However, the higher emission properties of InP/ZnS QDs could offer more energy transfer than InP QDs. This result is well consistent with Figure S1 and Table S1, Supporting Information.

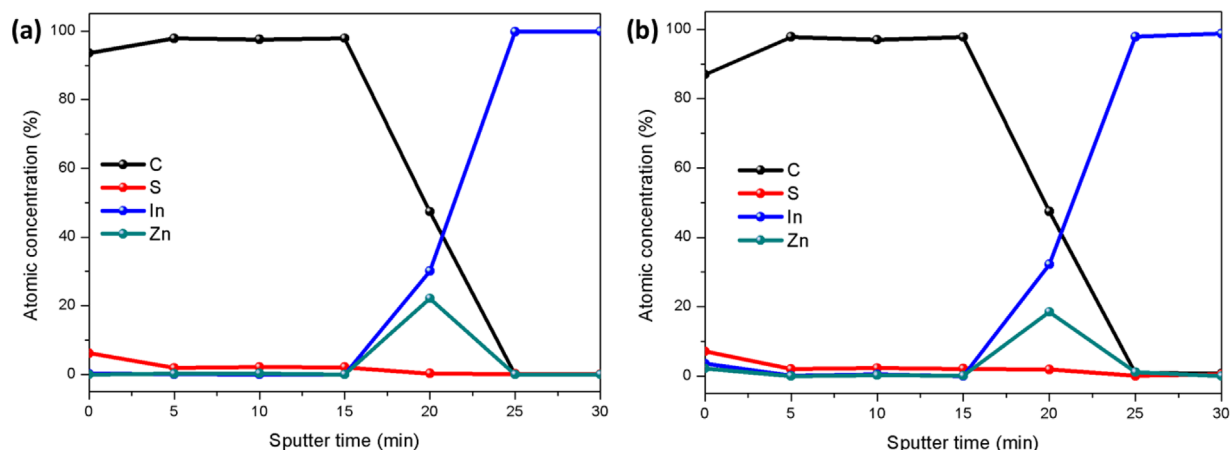


Figure 6. XPS depth-profiling characteristics of (a) BHJ active layer and (b) BHJ + QDs hybrid active layer.

Figure 6 shows XPS depth profiling characteristics of the devices fabricated (ITO/ZnO/active layer). Figure 6a shows the device fabricated with the BHJ active layer and Figure 6b shows the cross-section profile of the device fabricated with the BHJ + QDs active layer. Cross-section profiling was performed at $\approx 4 \text{ nm min}^{-1}$ from 0 min (top of active layer) to 30 min (bottom of active layer). The signals due to the measured atoms are expressed as atomic concentrations (%). In Figure 6a, carbon (C atom) and sulfur (S atom) signals from the molecular structures of PTB7-Th and PC₇₁BM appeared for ≈ 15 min (thickness was ≈ 60 nm). Subsequently, the C signal decreased rapidly and zinc (Zn atom) and indium (In atom) signals increased from the ZnO layer and ITO glass. On the other hand, Figure 6b showed meaningful In and Zn signals from 0 to 5 min, unlike Figure 6a. Thereafter C, S, In, and Zn signals appeared in the same order as in Figure 6a. This means that the InP/ZnS QDs were mostly distributed on the top surface (0 min) of the hybrid active layer.

InP/ZnS QDs had lower surface energy than PTB7-Th and PC₇₁BM (Figure S3, Supporting Information). Commonly, lower surface energy materials segregate at air/film interfaces, whereas higher surface energy materials segregate at film/electrode interfaces.^[58] Because of this property, when InP/ZnS QDs (with the lowest surface energy) were introduced to the BHJ active layer, they tended to distribute on the surface and the PTB7-Th and PC₇₁BM layers tended to be distributed under the surface of the BHJ active layer. As a result, InP/ZnS QDs were distributed on the surface of the BHJ + QDs active layer, contributing to improving the optical properties of the active layer. This tendency is consistent with the results in Figure 3–6.

Figure 7 shows GIWAXS characterization used to measure the crystalline structure of the hybrid active layer. The spectrum consists of out-of-plane and in-plane 2D patterns; the molecular packing and aggregation of films can be confirmed by GIWAXS analysis.^[59] The figures show the crystalline characteristics of pristine PTB7-Th (Figure 7a), the BHJ active layer (Figure 7b), PTB7-Th + InP/ZnS QDs (Figure 7c), and the BHJ + QDs hybrid active layer (Figure 7d). Also, Figure S4, Supporting Information shows line cut profile along q_z and q_{xy} axis. Pristine PTB7-Th showed a high intensity around $q_z = 2.0 \text{ \AA}^{-1}$ in the out-of-plane direction. This peak is due to the crystalline property of

PTB7-Th, which forms a highly π - π ordered structure on the substrate with mainly face-on orientation.^[60,61] The BHJ active layer film had a strong molecular ordering structure due to fullerene aggregation.^[62] When InP/ZnS QDs were incorporated in the pristine PTB7-Th, the intensity of $q_z = 2.0 \text{ \AA}^{-1}$ peak decreased and a strong crystalline peak was observed as a round shape above $q_z = 2.0 \text{ \AA}^{-1}$ by the aggregates of InP/ZnS QDs. Also, the new peak at $q_{xy} = 2.3 \text{ \AA}^{-1}$ was obviously formed by incorporating InP/ZnS QDs (Figure S4a, Supporting Information). Similar results were observed in Figure 7d: the BHJ + QDs active layer showed strong crystalline peak at $q_z = 2.0 \text{ \AA}^{-1}$ and $q_{xy} = 2.3 \text{ \AA}^{-1}$ resulted from aggregates of InP/ZnS QDs (Figure S4b, Supporting Information). These high crystalline characteristics of InP/ZnS QDs were in favor for enhancing

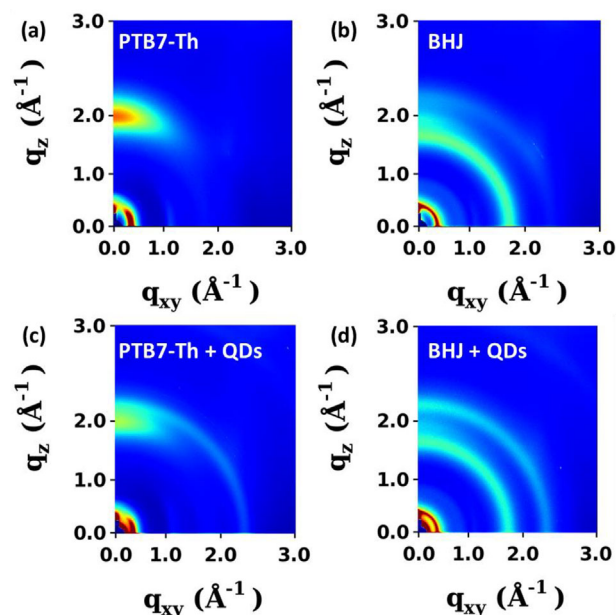


Figure 7. Grazing-incidence wide-angle X-ray scattering (GIWAXS) characteristics of (a) pristine PTB7-Th, (b) BHJ (PTB7-Th + PC₇₁BM), (c) PTB7-Th + InP/ZnS QDs, and (d) BHJ + InP/ZnS QDs.

charge transport result in enhancing performance of hybrid solar cells.

In particular, as shown in Figure 6, InP/ZnS QDs were distributed on the surface of the hybrid active layer, improving the optical properties. Further, the crystalline structure of the BHJ active layer was enhanced, as shown in Figure 7. As a result, InP/ZnS QDs improved the optical properties of the active layer via energy transfer and through distribution on the surface of the BHJ + QDs active layer to form a highly crystalline structured hybrid active layer. Through these two roles, the InP/ZnS QDs contributed to the improvement of J_{SC} in the fabricated devices. This is consistent with the improved J_{SC} results upon the introduction of InP/ZnS QDs, which is shown in Figure 3 and Table 1.

Figure 8 shows the AFM morphology characteristics of the hybrid active layer and ZnO layer. The root mean square (RMS) roughness was 1.819 nm when the BHJ active layer was introduced on the ZnO layer (Figure 8a) and 1.963 nm when the BHJ + QDs active layer was introduced on the ZnO layer (Figure 8b). The introduction of InP/ZnS QDs produced a rougher film. This is consistent with InP/ZnS QDs in the BHJ active layer being distributed on the surface of the hybrid active layer, as shown in Figure 6. RMS roughness values of 1.783 and 1.821 nm were observed when the BHJ active layer (Figure 8c) and BHJ + QDs active layer (Figure 8d) were, respectively, introduced on the EDT-modified ZnO layer. The introduction of

InP/ZnS QDs also formed a rougher film but the introduction of the EDT-modified ZnO layer formed a relatively uniform surface. This uniform surface contributed to enhanced carrier transport and reduced carrier recombination.^[63,64]

Figure 9 and Figure S5, Supporting Information show surface potential properties of the hybrid active layer and the ZnO layer. The surface potential of the ZnO layer was 498.747 mV ($R_q = 9.871$ mV) and that of the EDT-modified ZnO layer was 504.647 mV ($R_q = 5.520$ mV). The surface of the ZnO layer showed a higher and more uniform surface potential after EDT treatment. Song et al. reported that the surface potential of the ZnO layer increased after treatment with polar solvent, resulting in better electron extraction and transport (improved J_{SC} and FF).^[65] Thus, the ZnO layer with EDT treatment contributed to the improvement of J_{SC} and FF by providing a surface potential that was more suitable for electron extraction and transport, consistent with the results in Table 1.

The surface potential was 472.741 mV ($R_q = 6.293$ mV) when the BHJ active layer was introduced on the ZnO layer (Figure 9a) and 472.385 mV ($R_q = 6.227$ mV) when the BHJ + QDs active layer was introduced on the ZnO layer (Figure 9b). The introduction of InP/ZnS QDs showed lower and more uniform surface potential. In addition, the surface potential was 468.515 mV ($R_q = 5.845$ mV) when the BHJ active layer was introduced on the EDT-modified ZnO layer (Figure 9c) and 449.365 mV ($R_q = 4.961$ mV) when the BHJ + QDs active layer

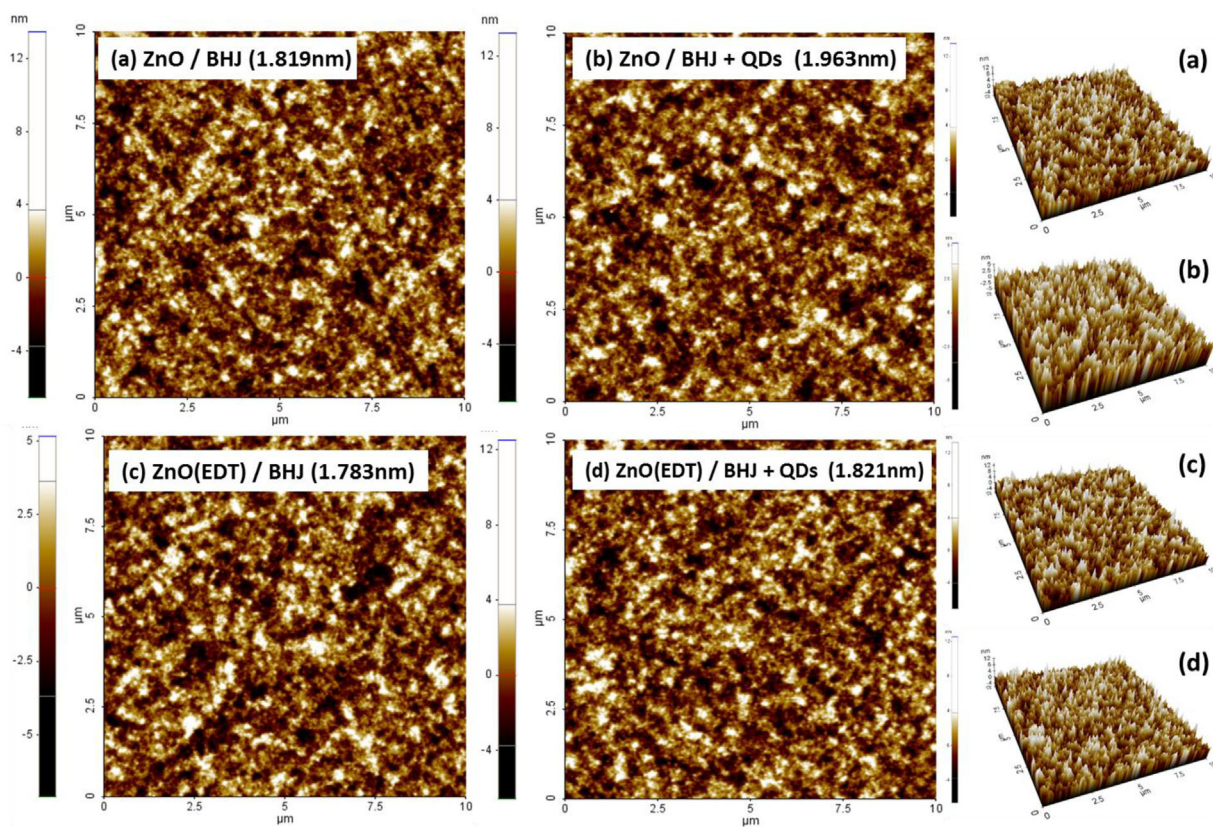


Figure 8. Morphology characteristics of (a) ZnO/BHJ, (b) ZnO/BHJ + QDs, (c) ZnO(EDT)/BHJ, and (d) ZnO(EDT)/BHJ + QDs (2D images in left and middle section, 3D images in right section).

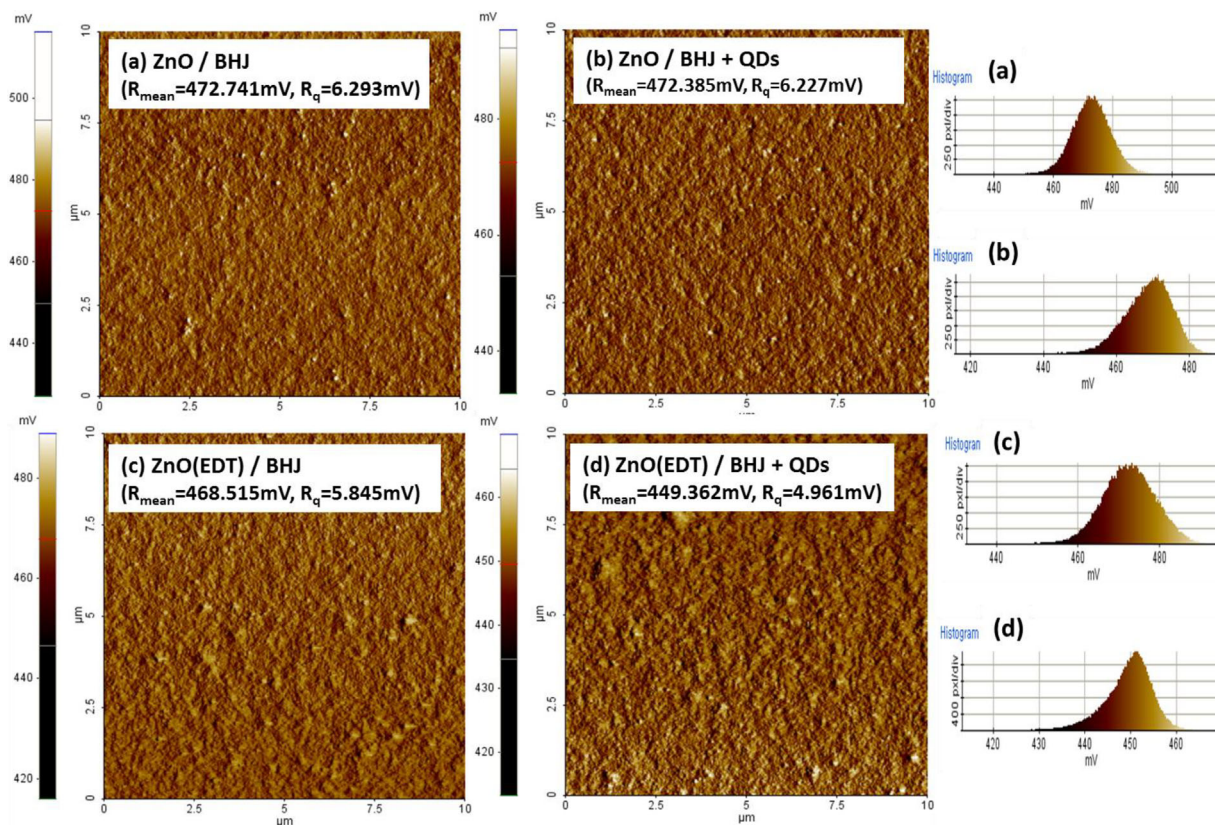


Figure 9. Surface potential characteristics of (a) ZnO/BHJ, (b) ZnO/BHJ + QDs, (c) ZnO(EDT)/BHJ, and (d) ZnO(EDT)/BHJ + QDs (2D images in left and middle section, histograms in right section).

was introduced on the EDT-modified ZnO layer (Figure 9d). The surface potential reduced significantly from 472.741 to 468.515 mV and a more uniform surface potential was observed at 6.293 mV from 5.845 mV due to introduction of the EDT-modified ZnO layer. This is a more uniform surface potential property than that due to the introduction of InP/ZnS QDs.

As shown in Figure 8, 9, and Figure S5, Supporting Information, when both InP/ZnS QDs and the EDT-modified ZnO layer were introduced, a uniform morphology (R_q : 6.293–4.961 mV) with low surface potential (472.741–449.362 mV) was observed. Compared to the surface potentials of the active layers and the high surface potential of the EDT-modified ZnO layer shown in Figure S5, Supporting Information, the EDT-modified ZnO layer (the highest surface potential) and the BHJ + QDs active layer (the lowest surface potential) were the most favorable for electron extraction and transport (shown in Figure S6, Supporting Information). The introduction of InP/ZnS QDs increased the optical properties of the hybrid active layer and enhanced the crystal structure. Introduction of the EDT-modified ZnO layer established uniform morphological properties, resulting in favorable structures for carrier generation and transport. Therefore, J_{SC} and FF could increase, which is consistent with the results in Table 1.

The morphological and surface potential characteristics of the devices containing InP QDs and the EDT-modified ZnO layer are shown in Figure S7, Supporting Information. Although the morphology was slightly roughened (1.819–1.838 nm) with

the introduction of InP QDs, the introduction of the EDT-modified ZnO layer caused a uniform morphology (1.838–1.793 nm). In addition, the surface potential decreased with the introduction

of InP QDs and the EDT-modified ZnO layer (472.741–467.468 mV), and the surface showed uniform properties (6.293–5.828 mV). However, the variations were smaller than those of Device 4 (with InP/ZnS QDs and the EDT-modified ZnO layer) and J_{SC} and FF were also lower. This result shows that the changes in the optical, morphological, and surface potential properties that resulted from the introduction of InP QDs had less effect on the device performance than the changes that resulted from the introduction of InP/ZnS QDs.

Hybrid ternary solar cells fabricated with InP/ZnS QDs enhanced the optical properties of the BHJ active layer. Energy transfer from the InP/ZnS QDs to the PTB7-Th polymer occurred due to the overlap between the absorption range (λ_{abs} = 550–800 nm) of PTB7-Th and the emission range (λ_{em} = 500–800 nm) of the InP/ZnS QDs. The InP/ZnS QDs used in this study passivated the surface defects of the core by introducing ZnS shells on the InP QDs (used in previous research), which resulted in increased emission relative to that of the InP QDs, thereby facilitating stronger energy transfer to PTB7-Th (shown in Figure 5). InP/ZnS QDs were distributed on the surface of the hybrid active layer (shown in Figure 6). Introduction of InP/ZnS QDs to the BHJ active layer caused a highly crystalline structure to be formed (shown in Figure 7). As

a result, the introduction of InP/ZnS QDs in the hybrid active layer increased carrier generation and transport by enhancing energy transfer and the crystallinity of the structure, thus improving J_{SC} of the fabricated devices. However, InP/ZnS QDs formed a rough morphology because they distributed on the surface and FF decreased (shown in Figure 3, 8, and Table 1). By introducing the EDT-modified ZnO layer, a more uniform film was formed (shown in Figure 8), which had lower and more uniform surface potential (shown in Figure 9). As a result, the trap sites of the ZnO layer were passivated, reducing carrier recombination, improving carrier transport, and improving both J_{SC} and FF of the fabricated devices (shown in Figure 3 and Table 1). As a result, the J_{SC} and FF of the device fabricated by the simultaneous introduction of InP/ZnS QDs and the EDT-modified ZnO layer were both greatly improved by the synergistic effect and a hybrid device exhibiting a high PCE of 10.2% was fabricated.

3. Conclusion

Hybrid ternary solar cells were prepared incorporating InP/ZnS QDs with noble absorption properties into PTB7-Th-PC₇₁BM-based BHJ active layer. InP/ZnS QDs were distributed on the surface of the hybrid active layer. InP/ZnS QDs have strong emission properties due to passivation of surface defects of InP core QDs by the ZnS shells. The InP/ZnS QDs transferred energy to PTB7-Th due to overlap between absorption band of PTB7-Th and emission band of InP/ZnS QDs, which enhanced photocurrent generation. InP/ZnS QDs-enhanced crystalline structures in the hybrid active layer resulted in enhanced carrier transporting properties. The EDT-modified ZnO layer provided uniform morphologies and surface potentials favorable for enhancing electron transport and reducing carrier recombination. Due to the synergistic effects of InP/ZnS QDs and the EDT-modified ZnO layer, the PCE of the hybrid ternary solar cell was 10.2%, resulting from the increased J_{SC} and FF.

4. Experimental Section

Materials: For the fabrication of hybrid solar cells, indium tin oxide (ITO) glass (sheet resistance of 10–15 Ω sq⁻¹) was purchased from AMG (Republic of Korea). Zinc acetate dihydrate [Zn(CH₃COO)₂·2H₂O, 99.999%], ethanolamine and 2-methoxyethanol (used as precursors for ZnO, 1,2-ethanedithiol (EDT) and acetonitrile (used as surface modification solvents for ZnO layer), and 1,8-diiodooctane (DIO) and chlorobenzene (CB) (used as solvents for the photoactive layer) were purchased from Sigma-Aldrich (USA). PTB7-Th and PC₇₁BM (used as photoactive materials) were purchased from 1-Material (Canada). InP/ZnS QDs (used as photoactive material) were purchased from Sigma-Aldrich.

Device Fabrication: To fabricate the hybrid ternary solar cells, ITO glass was cleaned by ultra-sonication using acetone, Alconox detergent, isopropyl alcohol, and D.I. water in sequence. After cleaning, the ITO glass was subjected to UVO treatment (Ahtech LTS AH 1700). The electron transport layer (ETL) (ZnO precursor) was spin-coated onto UVO-treated ITO glass at 3000 rpm for 30 s and annealed at 150 °C for 1 h. For ZnO surface modification, EDT (0.2 vol.% in acetonitrile) was spin-coated onto ZnO at 4000 rpm for 30 s. The BHJ active layer was formed with PTB7-Th and PC₇₁BM in the ratio 1:1.5 (25 mg mL⁻¹) in CB (DIO 3 vol.%). The hybrid BHJ active layer was formed with InP/ZnS QDs

(5 wt.%) in the BHJ active layer. The BHJ or hybrid BHJ active layer was pre-stirred at 60 °C in the glove box. The BHJ active layer was spin-coated to thickness of \approx 80 nm onto the ZnO or EDT-modified ZnO after filtering (0.2 nm polytetrafluoroethylene (PTFE) filter). The hole transport layer (HTL) (MoO₃) and metal electrode (Ag) were thermally deposited in a vacuum chamber (at 1×10^{-6} torr) at rates of 0.3 Å s⁻¹ (5 nm) and 2.0 Å s⁻¹ (100 nm), respectively. After fabrication, an encapsulation glass was attached using a UV sealant by UV curing for 3 min.

Film and Device Characterization: The current density–voltage (J – V) characteristics of the hybrid ternary solar cells fabricated were measured using a Keithley 2400 source meter. The light source used a solar simulator (Oriel, 100 mW cm⁻²) and the reference cell was calibrated at AM 1.5G. The external quantum efficiency (EQE) characteristics were measured using an IPCE measurement system (Mcsience, Polaronix K3100). The absorption properties and emission properties were measured using a UV-vis spectrometer (Agilent 8453) and a photoluminescence spectrometer (Perkin Elmer LS55), respectively. The sizes of the InP core QDs and InP/ZnS QDs were measured using transmission electron microscopy (TEM, JEM-2100). Time-resolved PL (TRPL) imaging was performed using an inverted-type scanning confocal microscope (MicroTime-200, Picoquant, Germany). The cross-section profile of BHJ and hybrid BHJ active layers were measured by XPS depth profiling (ULVAC-PHI 5000 VersaProbe, Phi (Φ)). The crystalline structures of BHJ and hybrid BHJ active layers were measured by GIWAXS. The surface morphology and surface potential characteristics were measured by AFM (PSIA XE-100) and EFM (PSIA XE-100 EFM). The contact angle and surface energy were measured by a contact angle analyzer (DSA100, KRÜSS).

Supporting Information

Supporting Information is available from the Wiley Online Library or from the author.

Acknowledgments

This research was supported by New and Renewable Energy Core Technology Program of the Korea Institute of Energy Technology Evaluation and Planning (KETEP) grant funded by the Ministry of Trade, Industry and Energy, Republic of Korea (no. 20153010140030) and the Human Resources Program in Energy Technology of the Korea Institute of Energy Technology Evaluation and Planning (KETEP), granted financial resource from the Ministry of Trade, Industry and Energy, Republic of Korea (No. 20174010201540).

Conflict of Interest

The authors declare no conflict of interest.

Keywords

electron transport layer, Förster resonance energy transfer, power conversion efficiency, quantum dots, surface potential, ternary solar cells

Received: March 19, 2018

Revised: May 10, 2018

Published online:

[1] Z. Li, K. Jiang, G. Yang, J. Y. L. Lai, T. Ma, J. Zhao, W. Ma, H. Yan, *Nat. Commun.* **2016**, *7*, 13094.

- [2] Y. Lin, F. Zhao, Y. Wu, K. Chen, Y. Xia, G. Li, S. K. K. Prasad, J. Zhu, L. Huo, H. Bin, Z. G. Zhang, X. Guo, M. Zhang, Y. Sun, F. Gao, Z. Wei, W. Ma, C. Wang, J. Hodgkiss, Z. Bo, O. Inganas, Y. Li, X. Zhan, *Adv. Mater.* **2017**, *29*, 1604155.
- [3] Y. Yan, X. Liu, T. Wang, *Adv. Mater.* **2017**, *29*, 1601674.
- [4] S. J. Jeon, S. J. Nam, Y. W. Han, T. H. Lee, D. K. Moon, *Polym. Chem.* **2017**, *8*, 2979.
- [5] E. J. Lee, J. P. Han, S. E. Jung, M. H. Choi, D. K. Moon, *ACS Appl. Mater. Interfaces* **2016**, *8*, 31791.
- [6] M. H. Choi, E. J. Lee, J. P. Han, D. K. Moon, *Sol. Energy Mater. Sol. Cells* **2016**, *155*, 243.
- [7] H. Yao, L. Ye, J. Hou, B. Jang, G. Han, Y. Cui, G. M. Su, C. Wang, B. Gao, R. Yu, H. Zhang, Y. Yi, H. Y. Woo, H. Ade, J. Hou, *Adv. Mater.* **2017**, *29*, 1.
- [8] Y. Liu, J. Zhao, Z. Li, C. Mu, W. Ma, H. Hu, K. Jiang, H. Lin, H. Ade, H. Yan, *Nat. Commun.* **2014**, *5*, 1.
- [9] M. Li, K. Gao, X. Wan, Q. Zhang, B. Kan, R. Xia, F. Liu, X. Yang, H. Feng, W. Ni, Y. Wang, J. Peng, H. Zhang, Z. Liang, H.-L. Yip, X. Peng, Y. Cao, Y. Chen, *Nat. Photon.* **2016**, *11*, 85.
- [10] H. Zhou, Y. Zhang, C. K. Mai, J. Seifert, T. Q. Nguyen, G. C. Bazan, A. J. Heeger, *ACS Nano* **2015**, *9*, 371.
- [11] C. Deibel, V. Dyakonov, *Rep. Prog. Phys.* **2010**, *73*, 96401.
- [12] S. Zhang, L. Ye, J. Hou, *Adv. Energy Mater.* **2016**, *6*, 1.
- [13] L. Chang, M. A. Holmes, M. Waller, F. E. Osterloh, A. J. Moulé, *J. Mater. Chem.* **2012**, *22*, 20443.
- [14] G. Li, R. Zhu, Y. Yang, *Nat. Photon.* **2012**, *6*, 153.
- [15] H. Lu, J. Zhang, J. Chen, Q. Liu, X. Gong, S. Feng, X. Xu, W. Ma, Z. Bo, *Adv. Mater.* **2016**, *28*, 9559.
- [16] N. Gasparini, X. Jiao, T. Heumueller, D. Baran, G. J. Matt, S. Fladischer, E. Spiecker, H. Ade, C. J. Brabec, T. Ameri, *Nat. Energy* **2016**, *1*, 16118.
- [17] J. Zhang, Y. Zhang, J. Fang, K. Lu, Z. Wang, W. Ma, Z. Wei, *J. Am. Chem. Soc.* **2015**, *137*, 8176.
- [18] S. Ten Cate, J. M. Schins, L. D. A. Siebbeles, *ACS Nano* **2012**, *6*, 8983.
- [19] X. Xu, Z. Li, Z. Wang, K. Li, K. Feng, Q. Peng, *Nano Energy* **2016**, *25*, 170.
- [20] C. Wang, X. Xu, W. Zhang, S. Ben Dkhil, X. Meng, X. Liu, O. Margeat, A. Yartsev, W. Ma, J. Ackermann, E. Wang, M. Fahlman, *Nano Energy* **2017**, *37*, 24.
- [21] H. Fu, Z. Wang, Y. Sun, *Sol. RRL* **2017**, 1700158, 1700158.
- [22] H. S. Shim, C. K. Moon, J. Kim, C. K. Wang, B. Sim, F. Lin, K. T. Wong, Y. Seo, J. J. Kim, *ACS Appl. Mater. Interfaces* **2016**, *8*, 1214.
- [23] Q. An, F. Zhang, Q. Sun, M. Zhang, J. Zhang, W. Tang, X. Yin, Z. Deng, *Nano Energy* **2016**, *26*, 180.
- [24] M. Zhang, J. Wang, F. Zhang, Y. Mi, Q. An, W. Wang, X. Ma, J. Zhang, X. Liu, *Nano Energy* **2017**, *39*, 571.
- [25] J. Wang, F. Zhang, J. Xiao, F. Li, M. Zhang, Q. An, J. Zhang, *J. Mater. Chem. C* **2016**, *4*, 7809.
- [26] T. Ameri, P. Khoram, J. Min, C. J. Brabec, *Adv. Mater.* **2013**, *25*, 4245.
- [27] Y. Xiao, H. Wang, S. Zhou, K. Yan, W. Xie, Z. Guan, S. W. Tsang, J. Bin Xu, *Nano Energy* **2016**, *19*, 476.
- [28] Q. An, F. Zhang, J. Zhang, W. Tang, Z. Deng, B. Hu, *Energy Environ. Sci.* **2016**, *9*, 281.
- [29] T. Liu, X. Xue, L. Huo, X. Sun, Q. An, F. Zhang, T. P. Russell, F. Liu, Y. Sun, *Chem. Mater.* **2017**, *29*, 2914.
- [30] Y. (Michael) Yang, W. Chen, L. Dou, W.-H. Chang, H.-S. Duan, B. Bob, G. Li, Y. Yang, *Nat. Photon.* **2015**, *9*, 190.
- [31] K. A. Mazzio, C. K. Luscombe, *Chem. Soc. Rev.* **2015**, *44*, 78.
- [32] W. Xu, F. Tan, X. Liu, W. Zhang, S. Qu, Z. Wang, Z. Wang, *Nanoscale Res. Lett.* **2017**, *12*, 11.
- [33] Y. Cheng, E. S. Arinze, N. Palmquist, S. M. Thon, *Nanophotonics* **2016**, *5*, 31.
- [34] G. H. Carey, A. L. Abdelhady, Z. Ning, S. M. Thon, O. M. Bakr, E. H. Sargent, *Chem. Rev.* **2015**, *115*, 12732.
- [35] M. V. Kovalenko, *Nat. Nanotechnol.* **2015**, *10*, 994.
- [36] L. Etgar, T. Moehl, S. Gabriel, S. G. Hickey, A. Eychmüller, M. Grätzel, *ACS Nano* **2012**, *6*, 3092.
- [37] X. Zhang, P. K. Santra, L. Tian, M. B. Johansson, H. Rensmo, E. M. J. Johansson, *ACS Nano* **2017**, *11*, 8478.
- [38] Z. Liu, Y. Sun, J. Yuan, H. Wei, X. Huang, L. Han, W. Wang, H. Wang, W. Ma, *Adv. Mater.* **2013**, *25*, 5772.
- [39] Z. Li, X. Zhang, C. Liu, Z. Zhang, Y. He, J. Li, L. Shen, W. Guo, S. Ruan, *J. Phys. Chem. C* **2015**, *119*, 26747.
- [40] Y. W. Han, E. J. Lee, J. Joo, J. Park, T. H. Sung, D. K. Moon, *J. Mater. Chem. A* **2016**, *4*, 10444.
- [41] A. Mohamed, Z. Karel, C. Pavel, M. E. Messing, P. Tonu, *J. Phys. Chem. Lett.* **2013**, *4*, 1760.
- [42] D. A. Wheeler, B. C. Fitzmorris, H. Zhao, D. Ma, J. Zhang, *Sci. China Chem.* **2011**, *54*.
- [43] M. Xia, C. Liu, Z. Zhao, J. Wang, C. Lin, Y. Xu, J. Heo, S. Dai, J. Han, X. Zhao, *Sci. Rep.* **2017**, *7*, 42359.
- [44] J. Park, S.-W. Kim, *J. Mater. Chem.* **2011**, *21*, 3745.
- [45] B. Zhang, Y. Wang, C. Yang, S. Hu, Y. Gao, Y. Zhang, Y. Wang, H. V. Demir, L. Liu, K.-T. Yong, *Phys. Chem. Chem. Phys.* **2015**, *17*, 25133.
- [46] J. J. Intemann, K. Yao, Y. X. Li, H. L. Yip, Y. X. Xu, P. W. Liang, C. C. Chueh, F. Z. Ding, X. Yang, X. Li, Y. Chen, A. K. Y. Jen, *Adv. Funct. Mater.* **2014**, *24*, 1465.
- [47] Z. Liu, X. Ouyang, R. Peng, Y. Bai, D. Mi, W. Jiang, A. Facchetti, Z. Ge, *J. Mater. Chem. A* **2016**, *4*, 2530.
- [48] S. Bai, Y. Jin, X. Liang, Z. Ye, Z. Wu, B. Sun, Z. Ma, Z. Tang, J. Wang, U. Würfel, F. Gao, F. Zhang, *Adv. Energy Mater.* **2015**, *5*, 1401606.
- [49] H. L. Yip, S. K. Hau, N. S. Baek, H. Ma, A. K. Y. Jen, *Adv. Mater.* **2008**, *20*, 2376.
- [50] P. Fu, X. Guo, B. Zhang, T. Chen, W. Qin, Y. Ye, J. Hou, J. Zhang, C. Li, *J. Mater. Chem. A* **2016**, *4*, 16824.
- [51] K. Feron, W. J. Belcher, C. J. Fell, P. C. Dastoor, *Int. J. Mol. Sci.* **2012**, *13*, 17019.
- [52] J.-S. Huang, T. Goh, X. Li, M. Y. Sfeir, E. A. Bielinski, S. Tomasulo, M. L. Lee, N. Hazari, A. D. Taylor, *Nat. Photon.* **2013**, *7*, 479.
- [53] Y. Zhu, L. Yang, S. Zhao, Y. Huang, Z. Xu, Q. Yang, P. Wang, Y. Li, X. Xu, *Phys. Chem. Chem. Phys.* **2015**, *17*, 26777.
- [54] C. Y. Chi, M. C. Chen, D. J. Liaw, H. Y. Wu, Y. C. Huang, Y. Tai, *ACS Appl. Mater. Interfaces* **2014**, *6*, 12119.
- [55] V. Gupta, V. Bharti, M. Kumar, S. Chand, A. J. Heeger, *Adv. Mater.* **2015**, *27*, 4398.
- [56] A. Sillen, Y. Engelborghs, *Photochem. Photobiol.* **1998**, *67*, 475.
- [57] P. Q. Bi, B. Wu, F. Zheng, W. L. Xu, X. Y. Yang, L. Feng, F. Zhu, X. T. Hao, *ACS Appl. Mater. Interfaces* **2016**, *8*, 23212.
- [58] S. Honda, H. Ohkita, H. Benten, S. Ito, *Adv. Energy Mater.* **2011**, *1*, 588.
- [59] W. Chen, M. P. Nikiforov, S. B. Darling, *Energy Environ. Sci.* **2012**, *5*, 8045.
- [60] Q. An, F. Zhang, J. Zhang, W. Tang, Z. Deng, B. Hu, *Energy Environ. Sci.* **2016**, *9*, 281.
- [61] S. Li, W. Liu, C.-Z. Li, T.-K. Lau, X. Lu, M. Shi, H. Chen, *J. Mater. Chem. A* **2016**, *4*, 14983.
- [62] P. Cheng, C. Yan, Y. Wu, J. Wang, M. Qin, Q. An, J. Cao, L. Huo, F. Zhang, L. Ding, Y. Sun, W. Ma, X. Zhan, *Adv. Mater.* **2016**, *28*, 8021.
- [63] K. D. Kim, D. C. Lim, J. Hu, J. D. Kwon, M. G. Jeong, H. O. Seo, J. Y. Lee, K. Y. Jang, J. H. Lim, K. H. Lee, Y. Jeong, Y. D. Kim, S. Cho, *ACS Appl. Mater. Interfaces* **2013**, *5*, 8718.
- [64] J. Chang, Y. Kuga, I. Mora-Seró, T. Toyoda, Y. Ogomi, S. Hayase, J. Bisquert, Q. Shen, *Nanoscale* **2015**, *7*, 5446.
- [65] B. R. Lee, E. D. Jung, Y. S. Nam, M. Jung, J. S. Park, S. Lee, H. Choi, S. J. Ko, N. R. Shin, Y. K. Kim, S. O. Kim, J. Y. Kim, H. J. Shin, S. Cho, M. H. Song, *Adv. Mater.* **2014**, *26*, 494.